Automated Transient Electromagnetic Data Processing for Ground-Based and Airborne Systems by a Deep Learning Expert System

Muhammad Rizwan Asif, Pradip K. Maurya, Nikolaj Foged, Jakob Juul Larsen, *Senior Member, IEEE*, Esben Auken, and Anders V. Christiansen

***Abstract*— Modern transient electromagnetic (TEM) surveys, either ground-based or airborne, may yield thousands of line kilometers of data. Parts of these data, especially in areas with dense infrastructure, are often disturbed by electromagnetic couplings due to infrastructure, e.g., power cables and fences. In most cases and in particular when working in a hydro-geological context, such coupled data must be culled before inversion. The process of identifying and culling coupled data is a manual task, requiring specialists to examine and process the data in detail. Manual data processing is subjective, difficult to reproduce, and time-consuming. To automate the complex data processing workflows, we propose an expert system based on a deep convolutional auto-encoder to identify couplings in the data. We configure the auto-encoder to learn an encoded representation of TEM data in a latent space. A reconstruction part that decodes the encoded representation is also trained, aiming to reconstruct input data. If the data unaffected by electromagnetic couplings are observed by the auto-encoder, the reconstructed output will have low error to the input. However, when having couplings in the data, the reconstruction error is elevated, indicating a nongeologic anomaly. The size of the anomaly is based on the relative error between the input data and the reconstructed output normalized by the data standard deviation. We show that the proposed approach displays high-quality data processing within a fraction of a second for a ground-based and an airborne system, which is either ready for inversion or requires minimal further quality inspection.**

***Index Terms*— Anomaly detection, convolutional neural network, data processing, deep learning, expert system, subsurface information, transient electromagnetics (TEM).**

I. Introduction

TRANSIENT electromagnetic (TEM) methods provide detailed images of the subsurface by uncovering variations in the electrical properties of subsurface conductivity. Such methods have been used for a variety of applications, including aquifer characterization [1], infrastructure planning [2], locating ground water extraction sites [3], and mineral exploration [4].

Modern TEM surveys, ground-based [5] or airborne [6], [7], [8], [9], yield large datasets that often contain thousands of line kilometers of data. Parts of these data, especially in areas with dense infrastructure, are often disturbed by electromagnetic couplings from man-made infrastructure, e.g., pipes, fences, power lines, telephone cables, and other underground cables.

The coupling phenomena arise when a TEM transmitter induces currents in a man-made conductive infrastructure. The responding signal (the coupling response) from the infrastructure is inherently synchronous with the Earth response. The measured data are, therefore, a coherent sum of the response from the Earth and the coupling response. The amplitude of the coupling response strongly depends on the size and shape of the man-made conductor, and the distance between the transmitter and the conductor [10]. The signature of couplings can appear as oscillatory (capacitive coupling), or as a smoother exponential decay superposed on to the Earth response (inductive couplings). The physics behind the coupling effects have been discussed in detail in the literature [10], [11], [12].

Couplings to infrastructure cause the data to be corrupted to a degree that cannot be corrected [13]. Therefore, the TEM data denoising approaches, such as [14] and [15], are not feasible. In most cases and in particular when working with hydro-geological models, a quasi-1-D geological layering is to be determined by the data. If such coupled data or their denoised counterpart are inverted, it creates spurious subsurface features, which heighten the risk of flawed geological interpretations and incorrect conclusions. Therefore, couplings in the data must be identified and culled prior to inversion.

Existing deep learning approaches for TEM data processing [16], [17] use supervised learning where labels from manually processed data from existing survey areas are used to train deep learning methods. However, manually processed data make the data-driven methods biased to local survey areas and limited geological conditions, which is infeasible for general deployment. Manually processed data also contain

Manuscript received 9 August 2022; revised 23 August 2022; accepted 24 August 2022. Date of publication 26 August 2022; date of current version 15 September 2022. This work was supported in part by Innovation Fund Denmark (IFD) through the Project "MapField" under Grant 8055-00025B and in part by "SuperTEM" under Grant 0177-00085B. *(Corresponding author: Muhammad Rizwan Asif.)*

Muhammad Rizwan Asif, Pradip K. Maurya, Nikolaj Foged, Esben Auken, and Anders V. Christiansen are with the Department of Geoscience and the Aarhus University Center for Water Technology (WATEC), Aarhus University, 8000 Aarhus, Denmark (e-mail: rizwanasif@geo.au.dk).

Jakob Juul Larsen is with the Department of Electrical and Computer Engineering and the Aarhus University Center for Water Technology (WATEC), Aarhus University, 8200 Aarhus, Denmark (e-mail: jjl@ece.au.dk).

Digital Object Identifier 10.1109/TGRS.2022.3202304

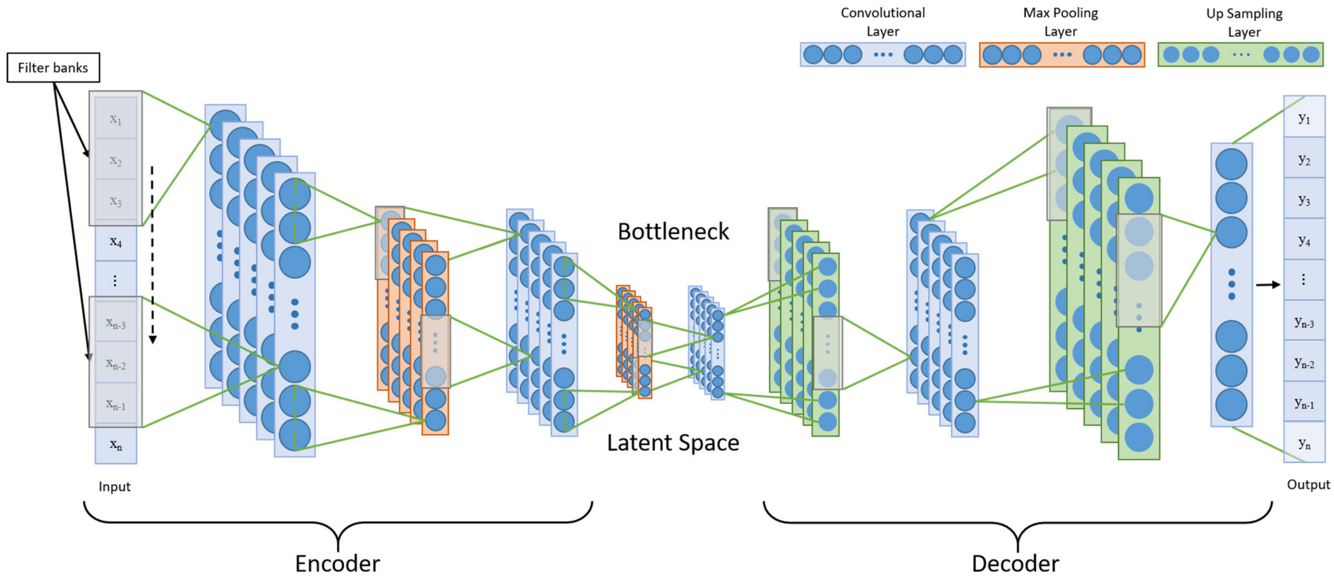

Fig. 1. Abstract representation of the convolutional auto-encoder used in this study.

irregularities, e.g., in the form of subjective inconsistent human labeling, which create additional complexities.

As of today, identification and culling of coupled data is mainly a manual and very tedious task, which requires specialists to examine the data in detail even though filters have been designed to support the culling of coupled data [18]. The manual data processing is even more challenging in areas with dense infrastructure where significant parts of the data can be corrupted.

To automate the complex data processing workflows, we present an alternative approach where identification of couplings is considered an anomaly detection problem. We deploy a deep convolutional auto-encoder-based expert system to differentiate couplings from uncoupled data (data not affected by couplings) in an automated manner. Since auto-encoders are unsupervised learning methods, we take the advantage of unlabeled data and make use of TEM data generated from a huge ensemble of 1-D subsurface models. The auto-encoder is configured and trained to learn an encoded representation of synthetic TEM data in a latent space. A reconstruction part is also trained that decodes the encoded data aiming to reconstruct the input data. If uncoupled data are observed by the auto-encoder, the reconstructed output will have low error to the input. However, when dealing with couplings, the reconstruction error will be elevated, which indicates an anomaly in the input data. We investigate the performance of the automated processing using our expert system on both ground-based and airborne TEM data, and compare it against the manual processing.

The remainder of this article is organized as follows. In Section II, we discuss the general methodology in detail. In Sections III and IV, we elaborate the methodology applied to a ground-based and an airborne system, respectively. We also compare the data processing and inversion results of the proposed automated approach with the standard manual workflows in Sections III and IV. We discuss the limitations and future prospects of the proposed scheme in Section V and give the conclusion remarks in Section VI.

II. General Methodology

Machine learning, especially deep learning methods, are powerful tools having the capabilities to extract distinct patterns from the data [19]. An auto-encoder is a special type of deep learning method that employs an encoder–decoder framework to learn efficient representation of unlabeled data [20]. The encoder extracts representative features from the input data, while the decoder reconstructs the input from the encoded representation. The data are generally encoded at the bottleneck layer, known as the latent space, which ensures learning of useful features instead of merely copying input to the output.

We use a convolutional auto-encoder where the network layers are composed of multiple convolutional layers. Convolutional layers have fewer learning parameters and leverage the idea of parameter sharing, sparse connectivity, and equivariant representations to ensure effective encoding of invariant features from the input data. By learning only the representative features from the data, anomalous data lead to high reconstruction error, which acts as an indicator for an anomaly. An abstract representation of our convolutional auto-encoder is shown in Fig. 1, while a detailed description of the network is given in Section III.

The convolutional layer can be defined as

$$h_{L+1}^{k} = \gamma\left(\sum_{j\in J} x_L^{j} \otimes w_L^{k} + b_L^{k}\right) \quad (1)$$

where h_{L+1}^{k} is the latent representation of k feature maps in the layer $L+1$, γ is the activation function, and x_L^{j} is the

jth feature map of the output in layer L. w_L^k and b_L^k are the kth filter weight and bias for the layer L, respectively, and $\otimes$ is the 1-D convolution operation. If the feature map x_L^j has the size W, filter has size F, and bias has size B, the output size of a convolutional layer will be $(W \times F + B)$ assuming a stride of 1.

The convolutional layer is generally followed by an activation function γ. A nonlinear γ reveals nonlinear correlations between the input features. In our case, we deploy the rectified linear unit (ReLu) given by

$$\gamma(x) = \begin{cases} 0, & x < 0 \\ x, & x \geq 0. \end{cases} \tag{2}$$

Our choice of a ReLu activation function is made because of its easy optimization advantages [21] and general purpose applicability [22].

For the encoder side of the bottleneck framework, we use the 1-D max-pooling layer following the convolutional and ReLu layers to downsample the input data by taking the maximum value over a window of a specified size. The pooling layers reduce the number of connections to the subsequent layer. The output shape of the pooling layer is given by

$$h_s = \frac{x_s - P_s}{S_s} + 1. \tag{3}$$

If x_s is the size of the input feature map, P_s is the pooling size, and S_s is the size of stride, h_s is the output size of the feature map.

To make a decoder from the latent space representation, we deploy a 1-D upsampling layer that repeats the temporal step P_s times and follows the convolutional layers. The weights in the convolutional layers ensure that the decoder reproduces the input data from the encoded representation.

We use the mean-squared error between the network input and the reconstructed output from the encoded representation as the loss function. To minimize the loss function for the training dataset, the network parameters are optimized by the Adam algorithm [23]. Additionally, an early stopping criterion [24], [25] is applied that ensures the network training is stopped when the loss function stops improving.

The input to the network is the observed TEM data d_{obs} while the output d_{NN} is the reconstruction of d_{obs} from the encoded representation by the auto-encoder. The idea is that if uncoupled TEM data are observed by the network, it will be able to reconstruct them with low error. However, if coupled data are observed, the reconstruction error will be elevated, which would indicate an anomaly in d_{obs}. In our case, we define a confidence metric as in the following equation:

$$C(\alpha) = \frac{1}{N}\sum_{i=1}^{N}[\varepsilon(i) < \alpha] \tag{4}$$

where

$$[\varepsilon(i) < \alpha] = \begin{cases} 1, & \text{if true} \\ 0, & \text{otherwise} \end{cases} \tag{5}$$

and

$$\varepsilon(i) = \frac{|d_{\text{NN}}(i) - d_{\text{obs}}(i)|}{\Delta d_{\text{obs}}(i)}. \tag{6}$$

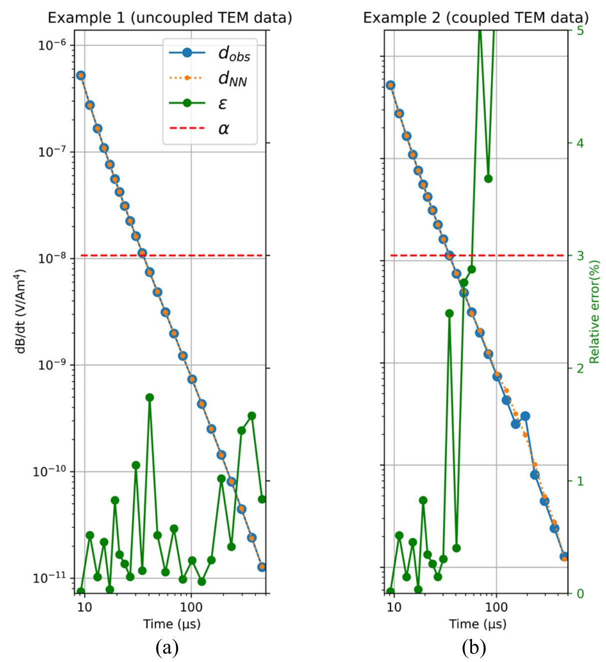

Fig. 2. Anomaly detection on synthetic data using the auto-encoder: (a) d_{obs} with no couplings and the reconstructed output d_{NN} shows low ε for each data point yielding in $C(3) = 24/24 = 1$ and (b) d_{obs} with synthetic anomaly at $\sim$200 μs, and the corresponding d_{NN} shows high ε indicating anomaly in d_{obs} and resulting a lower value of $C(3) = 14/24 = 0.58$.

The confidence metric (4) is based on the relative error ε between the input data d_{obs} and the reconstructed output d_{NN}, which is normalized by the data standard deviation Δd_{obs}. It counts the number of data points having relative error ε below a threshold α. The concept of (4) for an uncoupled synthetic TEM signal and its perturbed version representing a synthetic coupling is shown in Fig. 2.

For the examples shown in Fig. 2, the threshold α is set to 3 (indicated by red dashed line) and the number of data points N being evaluated is 24. Additionally, we assume $\Delta d_{\text{obs}} = 1$. In Fig. 2(a), uncoupled synthetic TEM data d_{obs} and its reconstructed output d_{NN} are shown. The relative error ε for all the data points is below the threshold α. In this case, $C(3) = 24/24 = 1$, yielding maximum confidence in the input data to be uncoupled. In Fig. 2(b), the TEM data are perturbed at the data point at $\sim$200 μs to represent a synthetic coupling. The relative error ε at late times is elevated, which yields a lower value of $C(3) = 14/24 = 0.58$, indicating an anomaly in the data.

The methodology presented in this section provides the basic framework. The specific methodology applied to the data from a ground-based [5] and an airborne [6] TEM system is discussed in detail in Sections III and IV, respectively.

III. Application to a Ground-Based TEM System

The ground-based towed TEM (tTEM) system [5] delivers images of the subsurface with depth, typically penetrating down to $\sim$100–120 m, and is capable of mapping 100–150 hectares per day. The tTEM system is a dual-moment system where the system records low moment (LM) and high

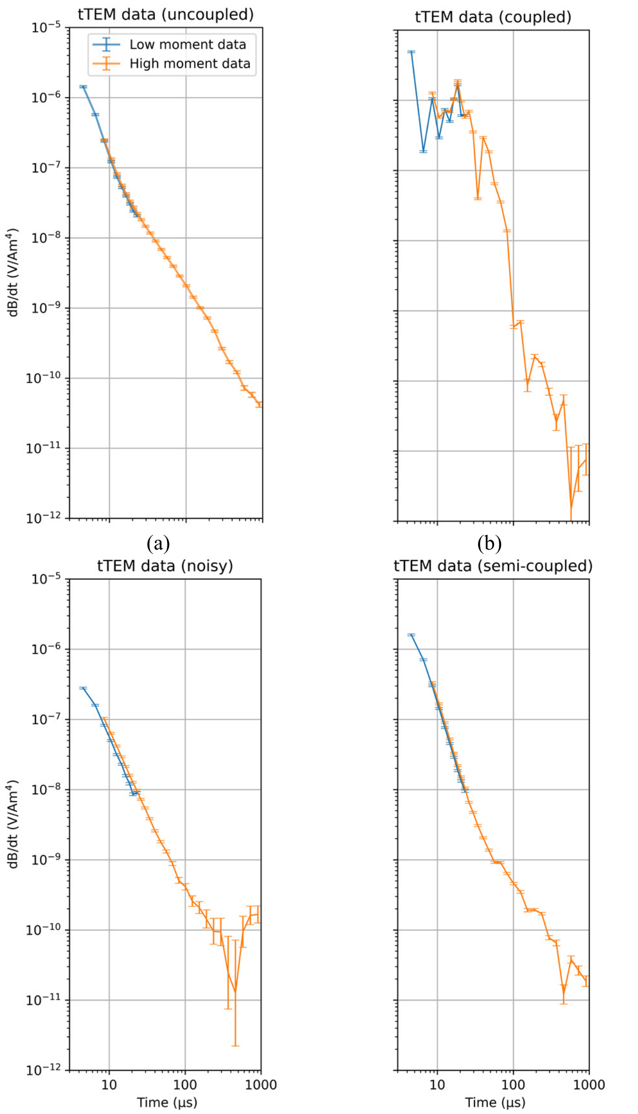

Fig. 3. Examples of tTEM raw data stacks: (a) data with no couplings; (b) coupled data; (c) data stack with random noise at late time data points indicated by high error bars; and (d) data stack with coupling in HM data from $\sim$50 μs onward.

moment (HM) data using two different current pulses. The measurement error, i.e., data uncertainty Δ, is calculated for each data point of a single raw stack by stacking several transient decays.

Fig. 3 shows four raw stacks of LM and HM data where the uncertainty Δ of each data point is represented by the error bars. Fig. 3(a) shows uncoupled data having small error bars, meaning a coherent signal. Couplings are also coherent by nature and, therefore, result in data with small error bars. It is observed in Fig. 3(b) until 300 μs. In addition, the late time data points in HM are usually affected by the random background noise and, therefore, associated with larger errors (especially see Fig. 3(c), HM gates after 200 μs). As such, the typical noise level in tTEM data is observed at around 1 nV/m^2. We also show a raw stack in Fig. 3(d) where the LM data are uncoupled, but couplings are observed in HM data points from $\sim$40 μs onward.

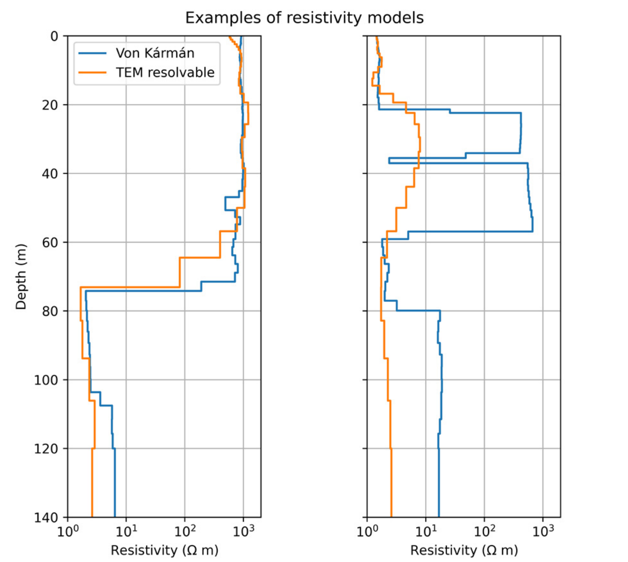

Fig. 4. Examples of resistivity structures generated by using von Kármán functions and the corresponding resistivity models when the TEM data of von Kármán models are inverted.

Evident from Fig. 3, the LM data hold few additional early data points compared to the HM for the tTEM system. Additionally, the LM and HM transmitter turn off times differ only by a few microseconds. Therefore, the effect of coupling is most often present in both the LM and the HM data. In the manual processing, for the abovementioned reasons, both LM and HM data are culled if a coupling is observed in HM data. For the automated processing, we only train one network for the HM data processing, and similar to the manual processing, we discard the LM data if a coupling is detected in the HM data.

A. Training Dataset

The training dataset consists of forward responses of TEM resolvable 1-D resistivity models ranging from 1 to 2000 $\Omega\cdot$m. The initial resistivity models are generated with 90 layers of exponentially increasing thicknesses, where the resistivity of each layer is chosen by using the broadband von Kármán covariance functions [26], [27] by varying resistivities, spatial distances, correlation lengths, and amplitudes. The resistivity models are chosen to have a top layer thickness of 1 m and a depth to last layer boundary at 120 m, which is the absolute maximum depth of investigation (DOI) of the tTEM system. The TEM responses of these models are inverted by using a standard least-squares inversion algorithm [28] to obtain geophysically resolvable models. As such, complex resistivity structures often produce TEM data that can be well-fit by simpler resistivity models. Two such examples are shown in Fig. 4 where the TEM response of the von Kármán resistivity structures is inverted to result in simpler resistivity models.

The process of generating the dataset of TEM resolvable models is explained in detail by Asif *et al.* [29], [30], and the dataset is publically available [30].

In total, one million forward responses are generated from resolvable 1-D resistivity models, which are sampled at

TABLE I
NETWORK CONFIGURATION

Layer Type	# of Filters	Filter Size	Output Shape
Input	-	-	(24,1)
Masking	-	-	(24,1)
Convolution	32	(3,1)	(24,32)
ReLu	-	-	(24,32)
Max Pooling	-	(2,1)	(12,32)
Convolution	32	(3,1)	(12,32)
ReLu	-	-	(12,32)
Max Pooling	-	(2,1)	(6,32)
Convolution	32	(3,1)	(6,32)
ReLu	-	-	(6,32)
Up Sampling	-	(2,1)	(12,32)
Convolution	32	(3,1)	(12,32)
ReLu	-	-	(12,32)
Up Sampling	-	(2,1)	(24,32)
Convolution	1	(3,1)	(24,1)

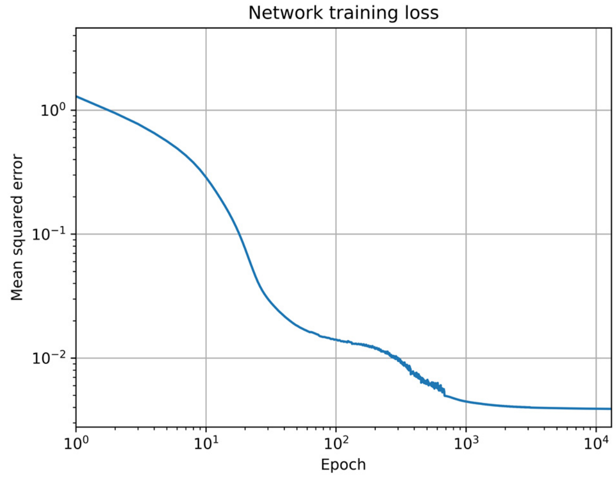

Fig. 5. Network training loss per epoch.

27 exponentially increasing time instants from $\sim$8 μs to $\sim$1 ms, similar to the HM time range of the tTEM system.

B. Network Configuration

We only want to investigate couplings and not random background noise, which result in higher Δ. Therefore, the data points after the time when Δ exceeds $\Delta_{\max}$ are masked at the input of the network to evaluate noise-free data. This is achieved by adding a masking layer where a mask value, set to zero, is used to skip data points for all succeeding layers.

The shape of the input layer corresponds to the first 24 data points of tTEM raw stack. We have not used all the data points, as the pooling layer requires the input data to return an integer representation when downsampled by the pool size P_s. We downsample the input features twice by a factor of $P_s = 2$ for an encoded representation of the input data. The encoded representation is decoded to the original dimension by an upsampling layer with the same step size used for downsampling. The detailed network configuration is shown in Table I.

To mimic the masking feature in the training dataset, a random data point is picked for each training sample from a uniform distribution, which is used to mask subsequent data points. Once the network is trained, it can be used for the evaluation of field data. The training loss of the network is shown in Fig. 5, where an epoch refers to one complete pass of the training dataset through the algorithm. The training takes a total of 13 121 epochs, and each epoch consumes $\sim$6 s of processing time on a NVIDIA GeForce RTX 2080 Ti GPU.

C. Expert System Algorithm

Given the trained network AE at T time instants, raw data stack RD(x, y) for x data points at t time instants and y number of raw stacks, data standard deviation $\text{RD}_\Delta(x, y)$, and a window size W, Algorithm 1 results in the output flags(x, y). The flags(x, y) gives a binary decision for each data point of the raw stack. In simple words, RD and RD_Δ are averaged over a window of $W = 7$ stacks to smooth out short-term fluctuations. To exclude the data points where the random noise overpowers the TEM signal, we find the first data point G_Δ that exceeds $\Delta_{\max} = 20\%$ to identify noise-free data, and assigned with a masking value to subsequent data points.

Algorithm 1 Algorithm for Field Data Evaluation for Couplings

```
Input: RD, RDΔ, W, AE, α, β_max, Δ_max
Output: flags
    Initialization:
  1.  for i = 1 to x-W step 1 do
        AD(:,i)= MovingMean[RD(:,i)] with W
        ADΔ(:,i)= MovingMean[RDΔ(:,i)] with W
        Find first gate GΔ in ADΔ(:,i) where ADΔ > Δ_max
        AD_mask(GΔ:end, i)= 0
        I_AE(:,i)= Interpolate(AD_mask) for T
        OP_AE(:,i)= AE[I_AE(:,i)]
        OP(:,i)= Interpolate[OP_AE(:,i)] for t
        Calculate C_i(α) for AD(:,i) and OP(:,i)
      end for
  2.  for j = 1 to x-(2W) step 1 do
          C_avg(j) = MovingMean[C_j] with 2W
          if C_avg(j) > β_max then
              flags(:, j) = 1
          else if C_avg(j) ≥ 0.80×β_max then
              flags(ε ≤ 1, j) = 1
          else
              flags(:, j) = 0
          end if
  3.  return flags
```

Since the time instants t at which the field data are recorded might differ for different surveys due to the TEM system calibration [31], the masked data points are linearly interpolated for the time instants T at which our network is trained on. The interpolated data points become the input to the AE. The output from AE is interpolated back to t, which is used to calculate the confidence value C using (4).

To highlight longer term trends, the confidence values C are averaged over a window size $2W$. The smoothened confidence values C_{avg} are used for a fuzzy decision-making process where all the data points of a raw stack are marked as coupled if C_{avg} has a low value. The data points of raw stacks with high value of C_{avg} are marked as uncoupled. However, for moderate C_{avg} values, only the data points having ε below 1 are marked as uncoupled. In our case, $\alpha = 2.5$ and $\beta_{\max} = 0.99$, which

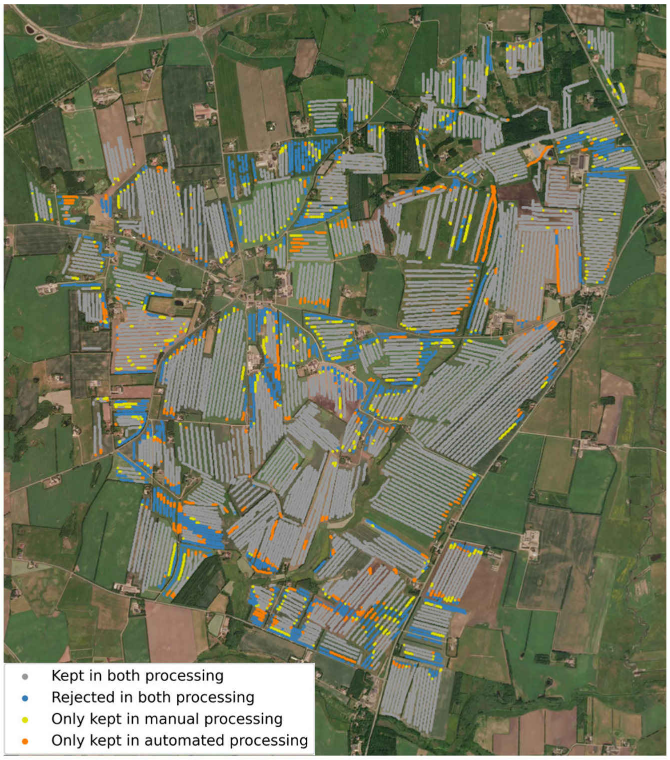

Fig. 6. Comparison of manual and automated data processing in the Aars survey area (showing ~5 km × ~4.4 km area).

describe the rigorousness of the automated processing. The parameters W, $\Delta_{\max}$, α, and $\beta_{\max}$ are discussed in detail in Section V.

D. Field Data Results

To show the performance of the proposed methodology, we apply it to a tTEM dataset acquired in northern Denmark, close to the town of Aars. The dataset was collected in 2019 covering an area of ~23 km^2 with 456 line kilometers of data (Fig. 6). The nominal line spacing is 25 m, and the driving speed is ~10–15 km/h. The couplings from raw data stacks were culled manually by an expert geophysicist using Aarhus Workbench [32]. The data culled by the geophysicist account for 22% of total raw stacks.

Fig. 6 shows the comparison of the proposed approach with the manual processing. The blue and gray points in Fig. 6 represent the data marked as coupled and uncoupled, respectively, by both processing schemes. The data locations at which the processing schemes disagree are indicated with orange and yellow points. The proposed approach keeps slightly more data stacks as compared to the manual processing and accounts for ~1% of total stacks. In general, there is a 96% agreement between the two processing schemes.

A visual inspection of a continuous ~60-s data stream and the comparison of processing are shown in Fig. 7, where all data points at one time instant yield a TEM curve similar to Fig. 3. We clearly observe couplings in the data centered at time instant 28 s in Fig. 7(a). This coupling pattern was identified by the manual operator and has been culled

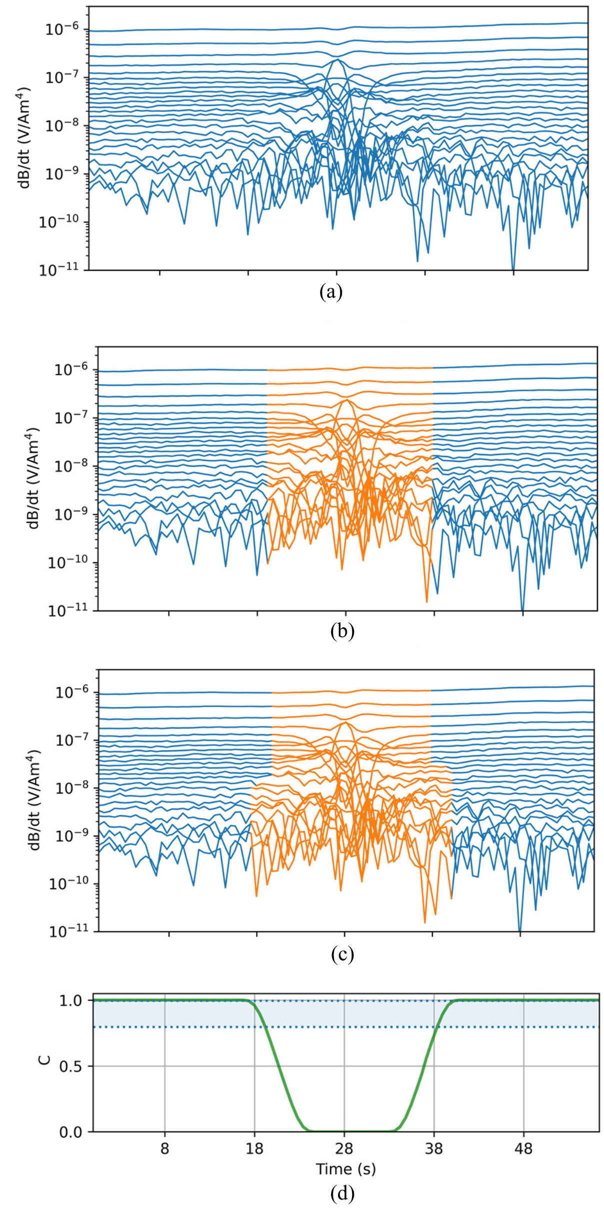

Fig. 7. Comparison of the manual and automated processing, where the orange region is marked as coupled—the data correspond to ~300 m distance: (a) field data stream; (b) manual processing; (c) automated processing; and (d) confidence metric for automated processing (highlighted area represents moderate values where fuzzy decision-making is performed).

[marked with orange in Fig. 7(b)]. The coupling was also detected by our proposed values obtained by (4), as in Fig. 7(d). As our approach flags each data point, the couplings are detected in an oblique manner.

A visual analysis of two more ~30-s data streams is shown in Fig. 8(a)–(h) where the manual and automated processing disagrees. Fig. 8(a) shows the raw data stack with some signatures of capacitive couplings; however, it is not detected in the manual processing [see Fig. 8(b)]. The automated processing result and the corresponding confidence values are shown in Fig. 8(c) and (d), respectively. The coupling signature is relatively clear from ~70 μs and onward as shown in the

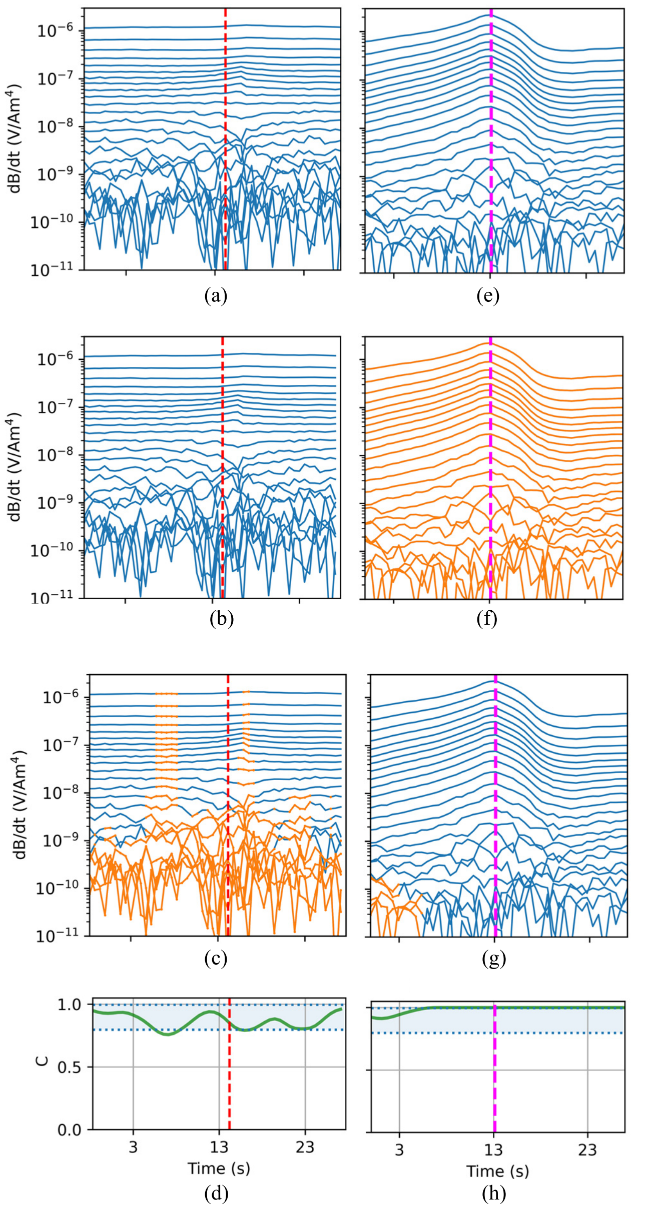

Fig. 8. Manual and automated data processing, where the schemes disagree. The orange region is marked as coupled: (a) and (e) field data streams; (b) and (f) manual processing; (c) and (g) automated processing; and (d) and (h) confidence metric for automated processing.

raw stack at the time instant ∼14 s in Fig. 9(a). The proposed strategy, however, keeps the data points until ∼40 μs (marked in green), which is before the coupling effect is observed.

On the other hand, Fig. 8(e) shows a data stream near a road. In such a scenario, some infrastructures, e.g., a buried power line, are excited by the tTEM transmitter, which shows signatures similar to strong inductive couplings [11]. The manual operator has removed all data in the vicinity of the road, as shown in Fig. 8(f). The automated approach cannot distinguish this type of coupling from uncoupled data, as the impact of this coupling appears as an enhanced signal level, which could easily be interpreted as a geological change in the signal (see Fig. 9(b) up until 70 μs where the raw stack at time instant ∼13 s is shown).

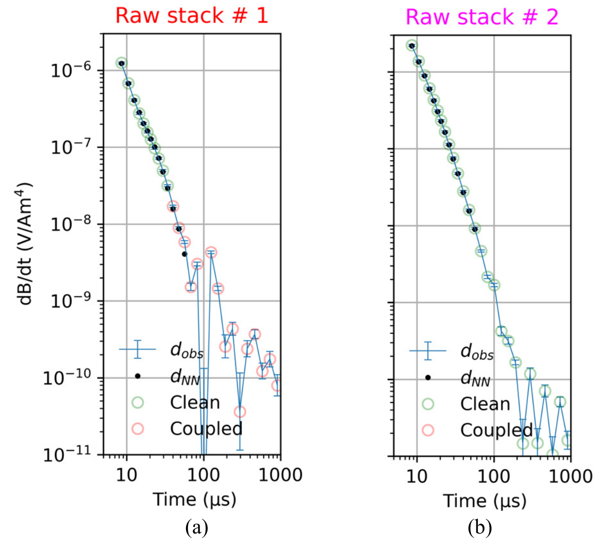

Fig. 9. Single raw data stack and network output for the vertical dashed lines (color coded by title) in data streams of Fig. 8: (a) raw data stack at time instant ∼14 s in Fig. 8(a) and (b) raw data stack at time instant ∼13 s in Fig. 8(b).

To compare the inversion results, we invert both datasets with the 1-D spatially constrained inversion algorithm [33] using AarhusInv [28]. We apply the commonly used settings with a 30-layer smooth model discretization with the starting layer boundary at 1 m and the last layer boundary at 120 m.

Both datasets are inverted with the same regularization strength, i.e., same vertical and horizontal roughness constraints. The constraints are set loosely so that the inverted models are mainly data-driven. Additionally, the data points exceeding 10% data uncertainty are excluded. Furthermore, the raw data stacks having less than seven usable data points after data processing are omitted. This decision is primarily based on the signal level and data quality of the survey. However, it is not the focus of this study, and the inversion settings remain the same for both processing schemes for one-to-one comparison. The manually processed data take 13 iterations to converge and result in a data misfit of 0.65. On the other hand, the automated processed data converge in 12 iterations and have a lower data misfit of 0.60. The data misfit φ, also known as data residual, is calculated as a least-squares difference between the observed data d_{obs} and modeled data $\text{F}(\mathbf{m})$ in a logarithmic space normalized with the data uncertainties Δd_{obs}, and is given in the following equation. Hence, a data residual of one corresponds to a fit to within one standard deviation of the data uncertainty

$$\varphi(\mathbf{m}) = \left(\frac{\left(\log_{10}(d_{\text{obs}}) - \log_{10}(F(\mathbf{m}))\right)^2}{\log_{10}(1+\Delta d_{\text{obs}})^2} \right)^{\frac{1}{2}}. \tag{7}$$

The inversion results for two profiles marked in Fig. 10(a) are shown along with the data misfit in Fig. 10(b) and (d) for the manual processing. The inversion results for the automated processing are shown in Fig. 10(c) and (e), and the data residual of most of the inverted models for both processing schemes is below one, which means that the modeled data

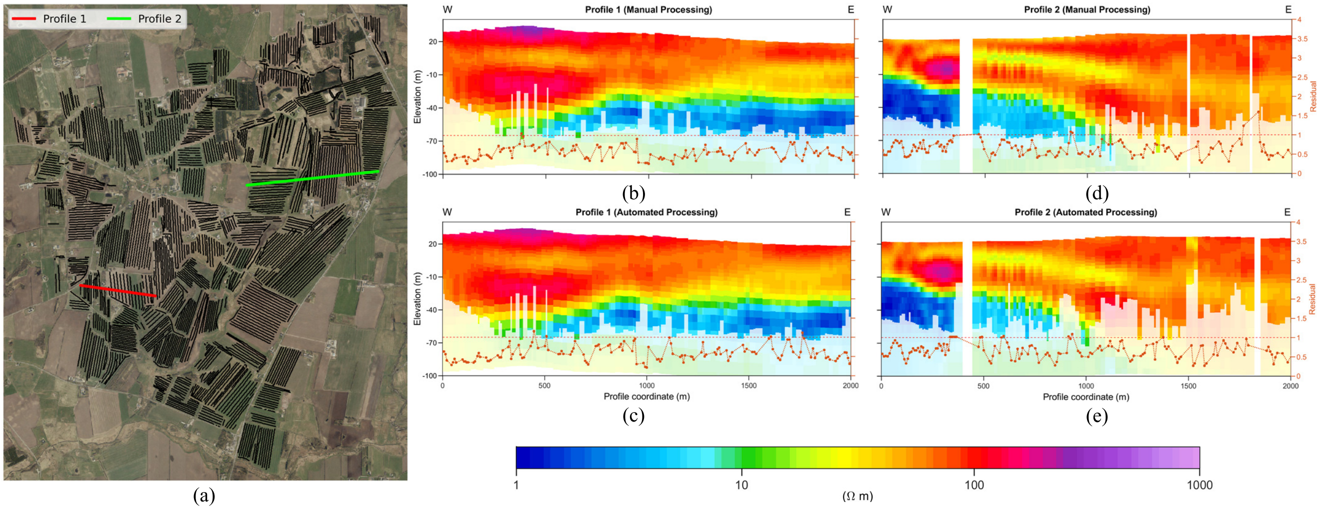

Fig. 10. Comparison of inversion for manual and automated data processing: (a) profiles; (b) and (d) inversion results for manual processing for profile 1 and profile 2, respectively; and (c) and (e) inversion results for automated processing for the corresponding profiles.

fit the observed data within the error bars. As expected, the resistivity models for both cross sections of the profiles in Fig. 10 are very similar in terms of the resistivity structure and DOI [34]. A minor difference is observed just before the gap in the resistivity section in profile 2 at coordinate ~480 m [see Fig. 10(d) and (e)]. The difference is caused by minor dissimilarities in the data culling of the couplings for the two processing schemes, causing gaps in the model section. The automated strategy keeps some early time data points, which results in a smaller gap, but with a shallower DOI for the models supported by early time data points. The manual processing is more conservative, and the operator has removed the raw data stacks completely, resulting in a slightly larger gap.

We also observe some differences in the resistivity section at profile coordinate ~1500 m in profile 2 [Fig. 10(d) and (e)]. The automated processing has kept some data here that were discarded in the manual processing. Since the data are kept in automated processing, a small anomaly in the resistivity section is observed. The anomaly could indicate an inductive coupling in the data not identified by the automated processing, as it can represent a geological change, like the example in Fig. 8(e). In this particular case, a residential facility is nearby, and the anomaly is most likely caused by an underground utility connection. However, there is no visual evidence of the cause of this coupling. This fits well with the experience that in many cases, the source of coupling cannot be visually identified, and may only be evident from the data.

In a geological context, the resistivity models in profiles 1 and 2 in Fig. 10 represent a two-layered structure, where the top resistive layer indicates a quaternary meltwater sand underlain by a low resistive prequaternary clay layer. A dipping thin clay layer is interbedded in the top sandy layer, as seen in profile 2.

IV. Application to an Airborne System

To apply the proposed methodology on an airborne TEM dataset, we use data from the SkyTEM system [6].

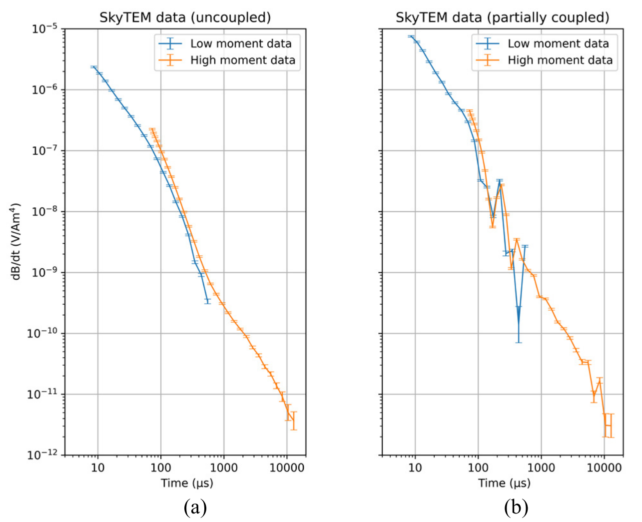

Fig. 11. Examples of SkyTEM raw data stacks: (a) data with no couplings and (b) data stack with couplings at late time data points in LM (50 μs onward) and in HM from 100 μs onward. Larger error bars are due to the random background noise.

The SkyTEM system typically images the subsurface down to 300–400 m. Similar to the tTEM, the SkyTEM system uses a dual-moment measurement acquisition scheme. However, in the SkyTEM case, the LM and HM waveforms are significantly different, and the LM and HM data span quite different time intervals, as shown in Fig. 11. The larger differences in the LM and HM data often result in couplings being observed in one of the moments only. Therefore, we need to train one network for the LM data and another one for the HM data.

A. Training Dataset

The process of generating the training dataset for the airborne system is similar to the approach given in Section III-A. For the resistivity models to be compatible with the SkyTEM system, we consider a top layer thickness of 4 m and a depth to last layer boundary at 500 m. In total, we generate one

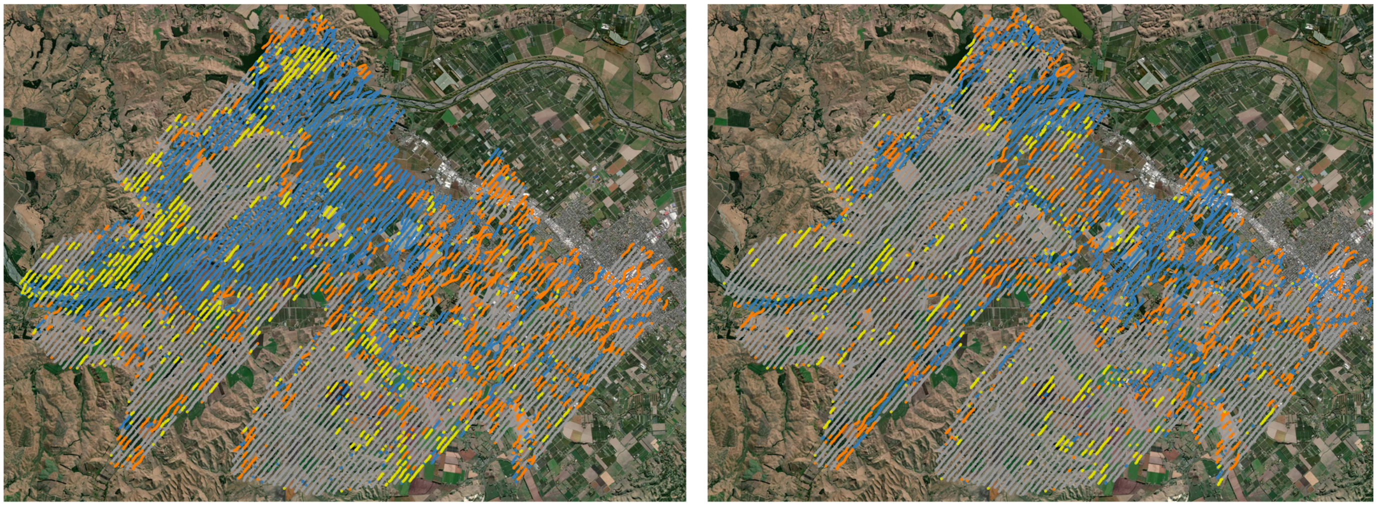

(a) (b)

Fig. 12. Comparison of manual and automated data processing (18 km × 23 km area): (a) processing comparison for LM data and (b) HM data processing results.

million forward responses, sampled between 10 and 350 μs for LM and 127 μs and 13 ms for HM, which is the typical time range of data from the SkyTEM system. Additionally, the flight altitude is uniformly chosen between 10 and 120 m for each model.

B. Network Configuration

The network configuration for the processing of HM data of the airborne system is kept the same as for the ground-based tTEM system, whereas the configuration for LM processing is slightly different due to fewer data points of LM data.

The shape of the input layer for the LM data processing corresponds to 16 data points of LM. The input shape is chosen to result in an integer representation during downsampling for the bottleneck of the network. The rest of the configuration remains the same.

The training loss of the LM and HM networks follows a similar trend as in Fig. 5. The LM network training takes a total of 14 699 epochs, and each epoch consumes ∼3.5 s of processing time while the HM network training takes a total of 21 824 epochs and consumes ∼6 s of processing time per epoch. The LM network training takes less time as compared to the HM network due to a lower number of data points at the input which reduces the total weights of the LM network.

C. Field Data Results

We use the same algorithm as presented in Section III-C to show the performance for the airborne system. Due to the sensitivity of the LM data to flight altitude, we choose $\beta_{\max} = 0.86$. We apply both networks for LM and HM data processing to a subset of the SkyTEM dataset acquired in Heretaunga Plains, located in the southern North Island of New Zealand. The Heretaunga SkyTEM survey was done in 2020 and holds ∼2600 line kilometers of data. In the manual processing, the culled LM data account for ∼28%, and the culled HM data account for ∼20% of total HM stacks.

Fig. 12(a) and (b) shows the comparison of performance for LM and HM airborne data, respectively. Similar to the tTEM processing results, automated data processing generally shows good agreement with manual processing and agrees for 84% for LM and 94% for HM data. The automated processing keeps ∼12% more LM data and ∼10% more HM data.

We show an approximately three-minute long data stream with LM data and corresponding flight altitude in Fig. 13(a) and (b). It is evident that a higher altitude generally results in lower signal level and a lower flight altitude results in a higher signal level. There is an obvious coupling between the time interval 30 and 60 s in the LM data [Fig. 13(b)], which is removed in the manual processing (marked in orange), as observed in Fig. 13(c). Additionally, some outlier data points, e.g., at times ∼150 and ∼160 s, have also been removed in the manual processing by the filters designed to assist data processing [18]. The result of the automated processing is shown in Fig. 13(d) based on the confidence metric given in Fig. 13(e). The proposed automated strategy results in lower confidence values for anomalous data and effectively identifies couplings between the time interval 30 and 60 s. However, it also removes some data stacks and data points at the outliers, e.g., at time ∼160 s.

For an inspection of HM data, we show a data stream and the corresponding flight altitude in the second column of Fig. 13. There are two obvious areas centered at ∼75 and ∼110 s where the HM data [Fig. 13(g)] are affected by couplings. The coupled HM data are removed by the manual operator (marked in orange) shown in Fig. 13(h). The automated approach also removes these anomalies effectively, observed in Fig. 13(i) based on the confidence values given in Fig. 13(j). It is evident from Fig. 13(j) that the coupled data result in lower confidence values.

To compare the inversion results for the automated and manually processed data, the airborne data are inverted using the same framework described in Section III. In this case,

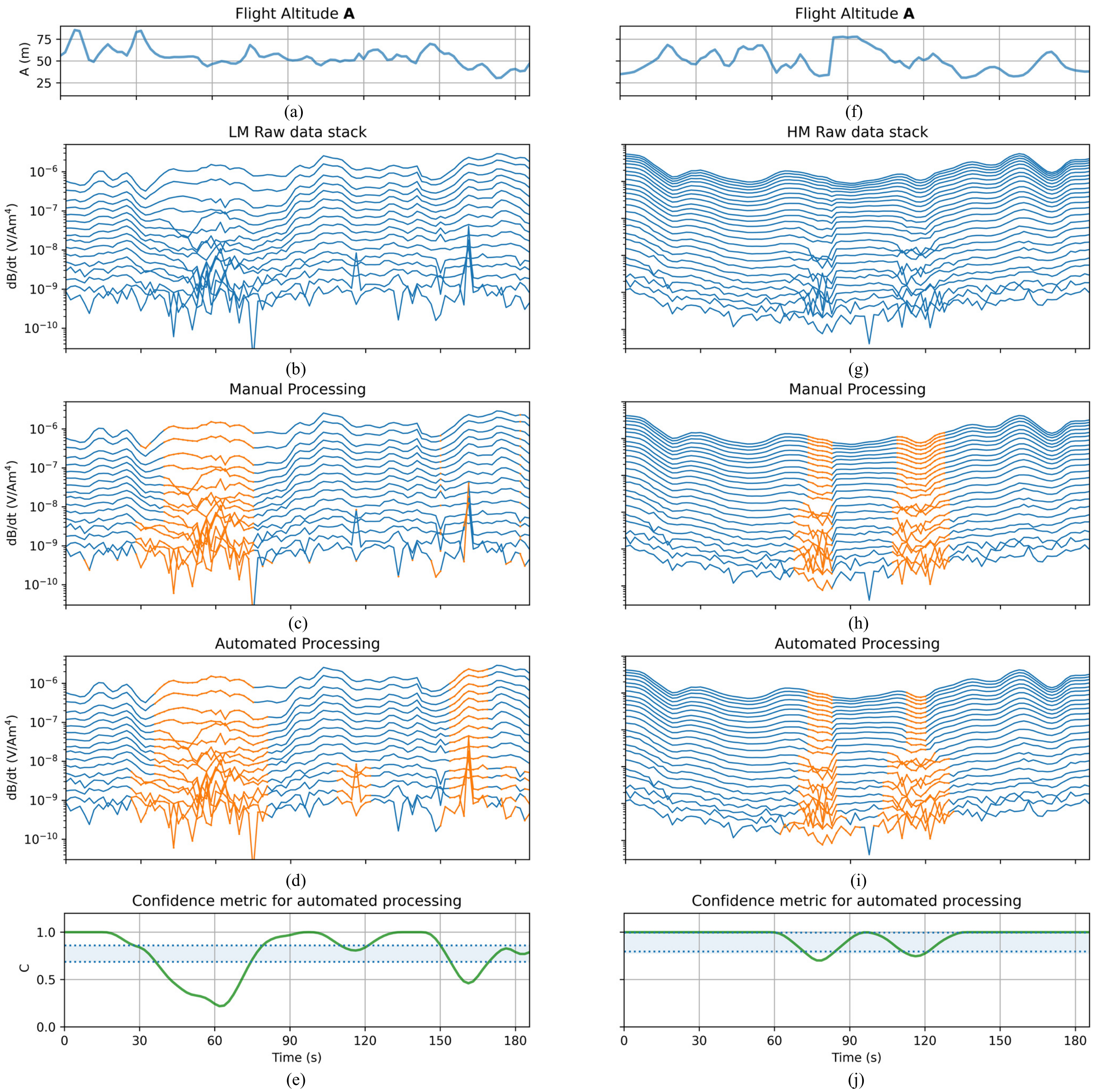

Fig. 13. Comparison of manual and automated data processing for LM and HM airborne data: (a) and (f) flight altitude of the airborne system; (b) and (g) raw data stacks; (c) and (h) manual processing; (d) and (i) automated processing; and (e) and (j) confidence metric for expert system decision-making.

the models are discretized from 4 to 500 m in depth, and data points exceeding 20% data uncertainty are excluded. Additionally, the raw data stacks having less than seven usable LM or HM data points after data processing were omitted prior to the inversion. The manually processed data take 16 iterations to converge and result in a total data misfit of 0.65. On the other hand, the automated processed data converge in 13 iterations with the same misfit.

The data processing results for another data stream are shown in Fig. 14(a) and (b), and the inversion results for the corresponding processed data are shown in Fig. 14(c) and (d), respectively. In general, there is a good agreement between the inversion results for both processing schemes. However, the proposed automated strategy keeps more early time data points at several instances, which results in more subsurface information with shallow DOI.

In a geological context, the top ~100 m in the central part of the section is the unconsolidated sediments followed by the basement. The unconsolidated sediments consist of a ~5-m top resistive sand layer followed by a ~10-m conductive clay layer and a ~90-m-thick high-resistive gravel layer. The basement reaches the surface in the southwest part while the boundary to the basement is unclear in the northeast part due to limited DOI.

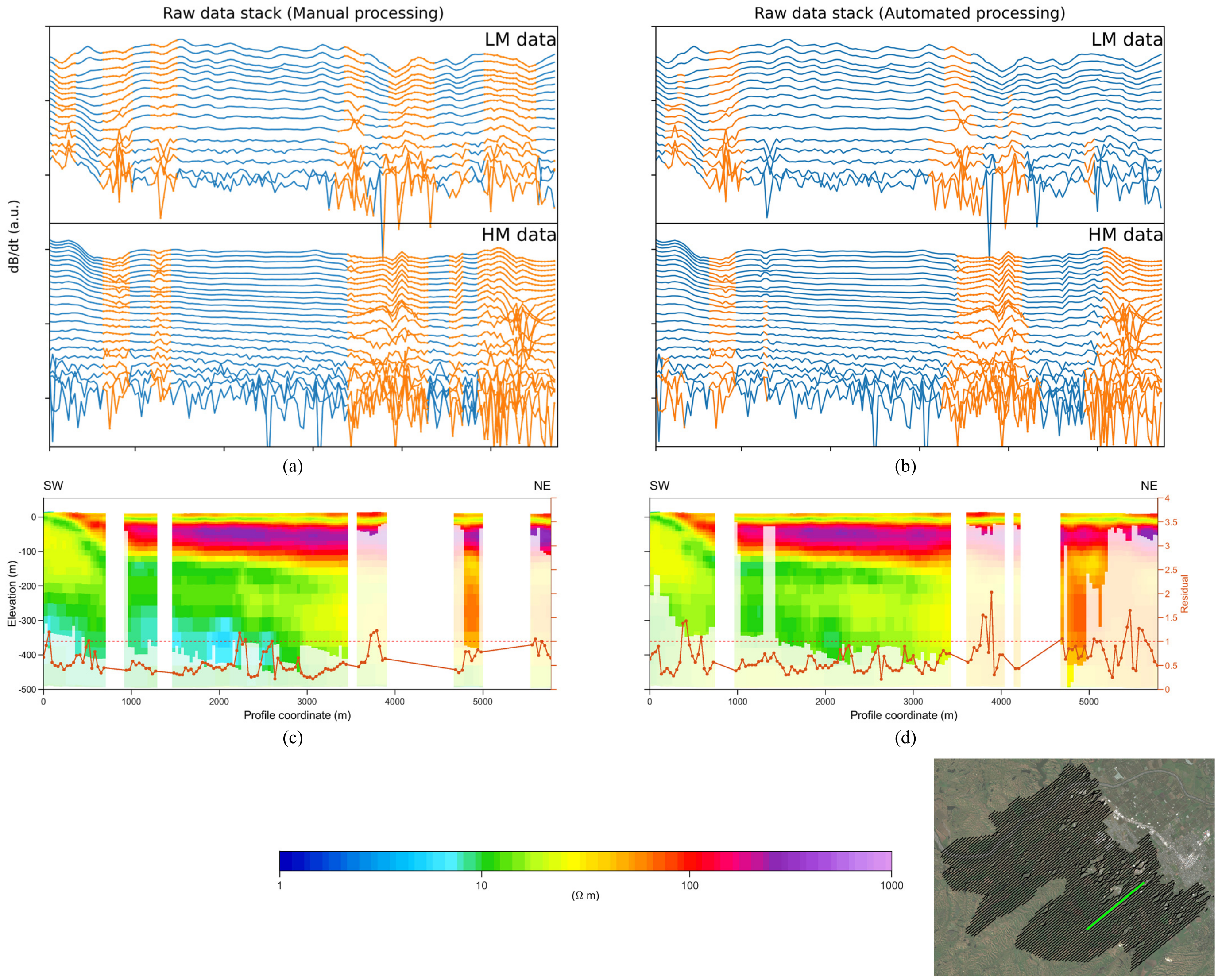

Fig. 14. Comparison of manual and automated processing for LM and HM airborne data, and the corresponding inversion results. The profile is shown in the map: (a) processing by manual operator; (b) automated processing; (c) inversion results for the corresponding manual data processing; and (d) inversion results for the corresponding automated data processing.

It should be noted that the raw data stacks in Fig. 14 are plotted over time (x-axis) while the resistivity models are shown on a distance x-axis. Due to variation in flight speed, some misalignments are observed between the data stacks and corresponding inversion results. As such, gaps in the resistivity section corresponding to the culled data stacks are not perfectly aligned.

V. Discussion

The inversion on the data processed by the proposed automated strategy takes fewer iterations to converge as compared to the manually processed data due to the improved handling of the couplings, especially in the ambiguous zones. As such, the footprint of the TEM system widens with depth; therefore, the signature of couplings generally appears in late time data points first and in early time data points afterward as the system approaches to the coupling source. On the contrary, when the system moves away from the coupling source, the coupling effect fades in early time data points first and in late time data points afterward. These ambiguous zones are dealt with appropriately due the fuzzy decision-making workflow where each data point is flagged as coupled or uncoupled for moderate values of C_{avg} (see Figs. 7 and 13). This is normally not done in manual processing, as it would make a tedious task even more challenging and time-consuming.

Our automated approach is unaffected by different properties of the man-made conductors, e.g., dimension and buried depth, that influence the amplitude of the coupling response. As long as the observed data cannot be represented by 1-D model parameters, the reconstruction error from the network is elevated, which indicates coupling in the data.

However, there are occurrences during a TEM survey when a coupling response mimics a geological response. If such data can be represented by 1-D model parameters, the autoencoder reconstructs the data with low error and the data will not be discarded. In these scenarios, the artifacts may be seen in the inverted data, which are also observed at ∼1500 m in Fig. 10(e). In scenarios where an anomalous-like geological pattern appears in the data close to any infrastructure, the data are conservatively culled by the manual operator to avoid any misrepresentation. Therefore, we see no anomaly in the inverted data processed manually [see Fig. 10(d)]. One could make use of remote sensing data, e.g., satellite maps, to locate infrastructure and remove data in its near vicinity.

If there are 2-D or 3-D effects in the data that cannot be represented by any 1-D resistivity model, a low confidence value may be obtained for such data, which consequently might be identified as an anomaly by our expert system. However, the data with 2-D or 3-D effects also require a different modeling framework. A future expansion of the data space incorporating data with 2-D or 3-D effects may enable its identification. To generate a 2-D or 3-D resistivity database, one would generate the initial von Kármán models as 2-D sections or 3-D volumes and use a 2-D or 3-D forward and inversion process, which of course would be much more computationally expensive compared to the 1-D case.

It is important for the proposed approach to have reliable data uncertainty estimates. For the SkyTEM and tTEM data used in the examples, the uncertainties for the data points for the raw stacks are estimated based on the standard deviation from the raw transients [5]. For moving TEM systems, e.g., the airborne SkyTEM and ground-based tTEM, it is important to have a relatively short raw stacking window to obtain good uncertainty estimates and to prevent the coupling signatures to be smeared, which would make the detection of the coupling more difficult. Further stacking of the TEM data can be applied after the automated data processing scheme to suppress the random background noise. Obtaining the raw data stacks and the corresponding data uncertainties is not trivial and may not be available for some TEM systems on the normal user/client level. In that case, the thresholds α and $\beta_{\max}$ may be empirically adjusted to obtain adequate processing results.

The automated processing involves several parameters, i.e., α, $\beta_{\max}$, W, and $\Delta_{\max}$. The thresholds α and $\beta_{\max}$ give an intuition about the leniency or strictness in the automated data processing. The window size W is used to smooth out short-term fluctuations in the raw data stacks. A larger value of W would smear the effect of couplings in the data. Additionally, $\Delta_{\max}$ identifies noise-free data and a smaller value means more certainty in the data. However, a higher value of $\Delta_{\max}$ may include some data points that are affected by the background noise. In that case, the values of ε for such data points will still be low due to their higher data uncertainty and they will be classified as uncoupled. These parameters are not very sensitive and can be adjusted in different ways to obtain similar data processing results.

Extensive testing on the data of several survey areas reveals that the same set of thresholds results in the best performance compared to the manual processing by searching for the best parameters by a grid-search method. This scenario may not be true if the signal levels are drastically low, e.g., in a very resistive case. In that case, the thresholds can be adjusted appropriately.

The proposed approach is fast and takes only 0.3 ms per raw data stack on an Intel Xeon Gold 6132 CPU at 2.60 GHz. Therefore, it can be incorporated directly in the TEM systems for real-time data processing. Our strategy is largely insensitive to the system transfer functions, e.g., system waveforms and low-pass filters in the receiver system, unless significant changes are made. The proposed method can easily be extended for other TEM systems by retraining on forward responses for those systems.

A small filter size in the convolutional layers ensures faster network training by reducing the computational complexity [35], and an odd number filter size symmetrically divides the previous layer data around the output. The chosen number of filters in the convolutional layers results in the best tradeoff between inference time and data reconstruction accuracy, and increasing the number of filters does not substantially increase the reconstruction accuracy.

The dimensionality of the latent space should ensure that only the useful features are learned instead of merely copying the input to the output. Our trained networks cannot reconstruct the data affected by couplings, which indicates that only the useful features are learned at the bottleneck. However, the dimensionality of the latent space can be reduced at the expense of increased reconstruction error.

We have only compared the automated processing against the manual processing. To the best of authors' knowledge, there are no other automated methods that would operate without training on a subset of the data from the specific survey area.

Our methodology is designed in a hydro-geological context. If the infrastructure that induces coupling response in the data is considered as exploration targets, a different strategy may be required where similar coupling patterns are identified. However, it is beyond the scope of this work and can be considered as future work.

VI. Conclusion

We have presented an automated approach to identify and cull couplings to infrastructure in ground-based and airborne TEM data. Due to the unsupervised learning strategy, our method is flexible to various survey areas and diverse geological conditions. The benefits of an automated and fast data processing approach are higher for electromagnetic surveys in areas with dense infrastructure where a major part of the data can be affected to couplings, and the manual data processing would be even slower. Our method is a significant step forward toward completely automated processing and inversion workflows to enable TEM methods to deliver the subsurface information in a time-efficient and cost-effective manner without the need for highly skilled specialists.

Acknowledgment

The authors would like to thank Aarhus Geo-Software (AGS), Aarhus, Denmark, for helping with importing of preprocessed data to Aarhus Workbench, and Hawke's Bay Regional Council (HBRC), Napier, New Zealand, and the Institute of Geological and Nuclear Sciences (GNS Science), Taupō, New Zealand, for providing access to the SkyTEM Surveys Aps, Aarhus, data from New Zealand.

REFERENCES

[1] E. A. White, C. D. Johnson, P. K. Maurya, W. Kress, D. B. Kelly, and J. W. Lane, "Use of a towed electromagnetic induction (tTEM) system for shallow aquifer characterization—An example from the Mississippi alluvial plain," in *Proc. Symp. Appl. Geophys. Eng. Environ. Problems*, May 2019, pp. 63–66.

[2] M. A. Kass, P. Maurya, T. Ingeman-Nielsen, J. Pedersen, S. Tomaskovicova, and A. V. Christiansen, "Towed transient electromagnetic survey results at ilulissat, Greenland for water vulnerability and infrastructure planning," in *Proc. NSG 2nd Conf. Geophys. Infrastructure Planning, Monitor. (BIM)*, 2021, pp. 1–5.

[3] H. Wiederhold, A. J. Kallesøe, R. Kirsch, R. Mecking, R. Pechnig, and F. Skowronek, "Geophysical methods help to assess potential groundwater extraction sites," *Grundwasser*, vol. 26, no. 4, pp. 367–378, Dec. 2021.

[4] Z. Guo, G. Xue, J. Liu, and X. Wu, "Electromagnetic methods for mineral exploration in China: A review," *Ore Geol. Rev.*, vol. 118, Mar. 2020, Art. no. 103357.

[5] E. Auken *et al.*, "TTEM—A towed transient electromagnetic system for detailed 3D imaging of the top 70 m of the subsurface," *Geophysics*, vol. 84, no. 1, pp. E13–E22, Jan. 2018.

[6] K. I. Sørensen and E. Auken, "SkyTEM—A new high-resolution helicopter transient electromagnetic system," *Explor. Geophys.*, vol. 35, no. 3, pp. 191–199, 2004.

[7] K. Kwan, A. Prikhodko, J. M. Legault, G. C. Plastow, J. Kapetas, and M. Druecker, "VTEM airborne EM, aeromagnetic and gamma-ray spectrometric data over the cerro quema high sulphidation epithermal gold deposits, Panama," *Explor. Geophys.*, vol. 47, no. 3, pp. 179–190, Sep. 2016.

[8] S. J. Balch, W. P. Boyko, and N. R. Paterson, "The AeroTEM airborne electromagnetic system," *Lead. Edge*, vol. 22, no. 6, pp. 562–566, Jun. 2003.

[9] A. P. Annan and R. Lookwood, "An application of airborne GEOTEM in Australian conditions," *Explor. Geophys.*, vol. 22, no. 1, pp. 5–12, Mar. 1991.

[10] K. I. Sørensen, E. Auken, and P. Thomsen, "TDEM in groundwater mapping—A continuous approach," in *Proc. 13th EEGS Symp. Appl. Geophys. Eng. Environ. Problems*, 2000, pp. 485–491.

[11] J. E. Danielsen, E. Auken, F. Jørgensen, V. Søndergaard, and K. I. Sørensen, "The application of the transient electromagnetic method in hydrogeophysical surveys," *J. Appl. Geophys.*, vol. 53, pp. 181–198, Oct. 2003.

[12] S. Kang, N. Dewar, and R. Knight, "The effect of power lines on time-domain airborne electromagnetic data," *Geophysics*, vol. 86, no. 2, pp. E123–E141, Mar. 2021.

[13] R. Kirsch, *Groundwater Geophysics: A Tool for Hydrogeology*. Berlin, Germany: Springer, 2006.

[14] S. Wu, Q. Huang, and L. Zhao, "De-noising of transient electromagnetic data based on the long short-term memory-autoencoder," *Geophys. J. Int.*, vol. 224, no. 1, pp. 669–681, Nov. 2021.

[15] F. Lin, K. Chen, X. Wang, H. Cao, D. Chen, and F. Chen, "Denoising stacked autoencoders for transient electromagnetic signal denoising," *Nonlinear Processes Geophys.*, vol. 26, no. 1, pp. 13–23, Mar. 2019.

[16] K. K. Andersen, C. Kirkegaard, N. Foged, A. V. Christiansen, and E. Auken, "Artificial neural networks for removal of couplings in airborne transient electromagnetic data," *Geophys. Prospecting*, vol. 64, no. 3, pp. 741–752, May 2016.

[17] T. Frederiksen and J. J. Larsen, "Detection of capacitive couplings in ground-based TEM data with a 1D convolutional neural network," in *Proc. 25th Eur. Meeting Environ. Eng. Geophysics*, 2019, pp. 1–5.

[18] E. Auken, A. V. Christiansen, J. H. Westergaard, C. Kirkegaard, N. Foged, and A. Viezzoli, "An integrated processing scheme for high-resolution airborne electromagnetic surveys, the SkyTEM system," *Explor. Geophys.*, vol. 40, no. 2, pp. 184–192, Jun. 2009.

[19] M. Reichstein *et al.*, "Deep learning and process understanding for data-driven Earth system science," *Nature*, vol. 566, pp. 195–204, Feb. 2019.

[20] M. A. Kramer, "Nonlinear principal component analysis using autoassociative neural networks," *AIChE J.*, vol. 37, no. 2, pp. 233–243, Feb. 1991.

[21] P. Ramachandran, B. Zoph, and Q. V. Le, "Searching for activation functions," 2017, *arXiv:1710.05941*.

[22] C. Bircanoglu and N. Arica, "A comparison of activation functions in artificial neural networks," in *Proc. 26th Signal Process. Commun. Appl. Conf. (SIU)*, May 2018, pp. 1–4.

[23] D. P. Kingma and J. Ba, "Adam: A method for stochastic optimization," 2014, *arXiv:1412.6980*.

[24] T. S. Bording *et al.*, "Machine learning based fast forward modelling of ground-based time-domain electromagnetic data," *J. Appl. Geophys.*, vol. 187, Apr. 2021, Art. no. 104290.

[25] M. R. Asif *et al.*, "A neural network-based hybrid framework for least-squares inversion of transient electromagnetic data," *IEEE Trans. Geosci. Remote Sens.*, vol. 60, pp. 1–10, 2021.

[26] A. V. Christiansen and E. Auken, "Layered 2-D inversion of profile data, evaluated using stochastic models," *ASEG Extended Abstr.*, vol. 2003, no. 1, pp. 1–8, Apr. 2003.

[27] I. Møller, B. H. Jacobsen, and N. B. Christensen, "Rapid inversion of 2-D geoelectrical data by multichannel deconvolution," *Geophysics*, vol. 66, no. 3, pp. 800–808, May 2001.

[28] E. Auken *et al.*, "An overview of a highly versatile forward and stable inverse algorithm for airborne, ground-based and borehole electromagnetic and electric data," *Explor. Geophys.*, vol. 46, no. 3, pp. 223–235, Sep. 2015.

[29] M. R. Asif *et al.*, "Integrating neural networks in least-squares inversion of airborne time-domain electromagnetic data," *Geophysics*, vol. 87, no. 4, pp. 1–54, 2022.

[30] M. R. Asif, N. Foged, T. Bording, J. J. Larsen, and A. V. Christiansen, "DL-RMD: A geophysically constrained electromagnetic resistivity model database for deep learning applications (dataset)," Zenodo, Aarhus, Denmark, Tech. Rep., 2022, doi: 10.5281/zenodo.6907090.

[31] N. Foged, E. Auken, A. V. Christiansen, and K. I. Sørensen, "Test-site calibration and validation of airborne and ground-based TEM systems," *Geophysics*, vol. 78, no. 2, pp. E95–E106, Mar. 2013.

[32] E. Auken, A. Viezzoli, and A. Christensen, "A single software for processing, inversion, and presentation of AEM data of different systems: The Aarhus workbench," *ASEG Extended Abstr.*, vol. 2009, no. 1, pp. 1–5, 2009.

[33] A. Viezzoli, E. Auken, and T. Munday, "Spatially constrained inversion for quasi 3D modelling of airborne electromagnetic data—An application for environmental assessment in the lower Murray region of South Australia," *Explor. Geophys.*, vol. 40, no. 2, pp. 173–183, Jun. 2009.

[34] A. Vest Christiansen and E. Auken, "A global measure for depth of investigation," *Geophysics*, vol. 77, no. 4, pp. WB171–WB177, Jul. 2012.

[35] A. Lavin and S. Gray, "Fast algorithms for convolutional neural networks," in *Proc. IEEE Conf. Comput. Vis. Pattern Recognit. (CVPR)*, Jun. 2016, pp. 4013–4021.

Muhammad Rizwan Asif received the B.S. degree in electrical (telecommunication) engineering from COMSATS University Islamabad (CUI), Islamabad, Pakistan, in 2013, and the M.S. and Ph.D. degrees in information and communication engineering from Xi'an Jiaotong University, Xi'an, China, in 2016 and 2019, respectively.

Since then, he has been working as a Post-Doctoral Researcher with the Department of Geoscience and the Department of Electrical and Computer Engineering, Aarhus University, Aarhus, Denmark, where he is currently a Researcher with the HydroGeophysics Group (HGG), Department of Geoscience, and supports research projects employing electrical and electromagnetic methods. His research interests include machine-learning applications for geophysical data. He is also interested in image processing and computer vision for intelligent automated systems.

Pradip K. Maurya received the Ph.D. degree in direct current resistivity and induced polarization (DCIP) method, Aarhus University, Aarhus, Denmark, in 2017.

He is currently an Assistant Professor with the HydroGeophysics Group, Aarhus University, Aarhus, Denmark. Apart from the DCIP method, his research also focuses in the field of airborne and ground-based electromagnetic methods for near-surface applications. He has a vast experience in data processing and inversion of electrical and electromagnetic data. He has also a strong interest in the development of geophysical instruments and is currently involved in the development of the towed transient electromagnetic (tTEM) instrument.

Nikolaj Foged received the M.Sc. and Ph.D. degrees in geology/geophysics from Aarhus University, Aarhus, Denmark, in 2001 and 2014, respectively.

He is currently a Senior Geophysicist with more than 20 years of employment with the HydroGeophysics Group (HGG), Department of Geoscience, Aarhus University. He has excessive experience in processing, modeling, calibration, etc., of airborne and ground-based electromagnetic (EM) data. His research is also focused on the integration of the geophysical mapping results in the development of geological and hydro-stratigraphic models. He has hands-on experience in all the workflows from EM-data collection in remote places to compiling the final hydro-stratigraphic/geological model output from large-scale airborne EM surveys.

Jakob Juul Larsen (Senior Member, IEEE) was born in Denmark, in 1973. He received the M.Sc. and Ph.D. degrees in experimental physics from Aarhus University, Aarhus, Denmark, in 1998 and 2000, respectively.

From 2000 to 2013, he held research and teaching positions in private and public companies. Since 2013, he has been with the Department of Electrical and Computer Engineering, Aarhus University, where he holds a position as Associate Professor. He works with geophysical instrumentation, signal processing, and machine learning. His current research interests are the domains of magnetics, transient electromagnetics, direct-current-induced polarization, and surface nuclear magnetic resonance.

Esben Auken received the M.Sc. and Ph.D. degrees in geophysics from Aarhus University, Aarhus, Denmark, in 1991 and 1996, respectively.

He is currently a Professor of Geophysics with the Department of Geoscience, Aarhus University, where he has led a big research team (the Hydro-Geophysics Group, HGG) consisting of 25–30 scientists all working with electrical and electromagnetic methods for high-resolution mapping of the shallow subsurface with focus on surface and groundwater processes. He has also served as the Vice-Director of the Geological Survey of Denmark and Greenland (GEUS). He is a Co-Founder of SkyTEM Surveys Aps, Aarhus Geo-Software, Aarhus, and Aarhus Geo-Instruments, Aarhus, all spin-out companies from the research group. The focus areas are surface nuclear magnetic resonance, ground-based and airborne transient electromagnetic (TEM), and surface, cross borehole direct current, and induced polarization. His research interests include mapping, compilation, and storage of data, research, monitoring, and consultancy within water, energy, minerals, and climate and environment.

Anders V. Christiansen received the Ph.D. degree in airborne transient electromagnetic (TEM) methods and inversion methodologies, Aarhus University, Aarhus, Denmark, in 2003.

He is currently a Professor with the Department of Geoscience, Aarhus University, Aarhus, Denmark, and is currently leading the Hydrogeophysics Group (HGG), which consists of 25–30 scientists. Overall, his research focus remains within airborne TEM methods and inversion methodologies. In the later years, he has an increased focus on the integration of various data types (e.g., geophysics with borehole information and hydrological observations) with the purpose of making objective and transparent processes that generate maps and other outputs that are in better agreement with the actual needs of the end users.